



# On the Electromagnetic Diffraction Propagation Model and Applications

Songlin Li , Guolong Cui , Senior Member, IEEE, Shisheng Guo, Member, IEEE, Chao Jia, Lingjiang Kong, Senior Member, IEEE, and Xiaobo Yang

**Abstract**—Detection and localization of nonline-of-sight (NLOS) hidden target in complex urban environment is a very recent radar detection problem. In this article, we investigate the possibility of locating a target in a building corner NLOS region with a single-input single-output ultra-wideband radar by exploring the electromagnetic (EM) diffraction propagation path. The EM wave diffraction phenomenon referring to this single rectangular corner of the building is analyzed and the diffraction model in this scenario is established. Assuming that the geometric structure of the scenario is known earlier, we introduce an application of the destination location behind the corner based on the propagation of the EM wave diffraction. Finally, the numerical simulation and real data results demonstrate that a micromotion target and moving target can be localized exploiting the proposed approach.

**Index Terms**—Electromagnetic (EM) diffraction propagation, nonline-of-sight (NLOS) signal, target localization, urban environment, ultra-wideband (UWB) radar.

## I. INTRODUCTION

THE DETECTION of the hidden target in urban environment is of great interest in both military and civil security fields, such as urban battles, antiterrorism actions, and disaster rescues. However, unlike the applications of the traditional radars, which detect the targets within the line-of-sight (LOS) scale. Thus, detecting a non-LOS (NLOS) target is a challenging work, especially for the complex urban environment sensing, and has been receiving more and more attentions.

Although the wall detection is a typical urban NLOS target detection method, as the name suggests, the location information of the NLOS targets are acquired by electromagnetic (EM) penetrating signals. In [1]–[3], multipath exploitation is applied to through-the-wall radar (TWR) imaging and urban sensing. In [4]–[6], several multipath suppression algorithms based on TWR are proposed in multipath environment. The detection with the TWR works well for only a single wall. However, because

the EM wave will be refracted when it penetrates through the wall, results in the target position shift and defocus the image. In particular, the multipath caused by multibounce echoes that are reflected and diffracted by a target and its surroundings is usually a nuisance signal for the through the wall radar systems, which is liable to cause false targets. Moreover, when the EM wave penetrates the whole room or building corner, the penetrating signals are very weak because of the strong attenuation. As a result, detection of targets hidden behind the corner of the building by the penetrating signal will be severely limited.

To detect the hidden target behind the corner of the building, several methods that exploit the reflection and corner diffraction signals are gradually developed [7]–[13]. Swedish Defence Research Agency (FOI) initiated a project entitled “Radar for detection of human activities around corners,” and carried out a series of research works about detection of target behind a corner. Specifically, literatures [7]–[9] provided the target range profile results of a real experiment conducted in multipath propagation environment. Two localization algorithms for locating of targets behind corners using an X-band radar were presented in [10] and [11], respectively. In addition, they extracted the microdoppler signature of human and unmanned aerial vehicle behind the corner of the wall using a “sensing-behind-the-corner” radar [12], [13].

In some other works [14]–[19], multipath exploitation was investigated in the urban environment. Multipath was considered in [14] for a synthetic aperture radar with a ground-based L-band radar. Two multipath exploitation target imaging techniques were proposed based on two different geometry city models (urban canyon scenario and T-junction scenario). The real data results aiming at exploiting multipath information are presented in [15] for airborne multipath exploitation radar technologies. In [16], a target position estimation algorithm based on multipath tracking of first-order reflection path was proposed. In [17], the generalized likelihood ratio test particle filter is employed to provide the most efficient NLOS targets localization results. In [18] and [19], Thai *et al.* carried out the work of detecting and locating targets in NLOS areas with a single portable radar by exploiting reflection multipath. In [18], an around-the-corner hidden target localization algorithm based on multipath subspace matched filter by using a portable millimeter-wave radar was proposed. Based on the previous work, they proposed two algorithms, which handle the information provided by multipath returns in different ways to detect and estimate the NLOS target position in [19]. In the present article, we also

Manuscript received September 14, 2019; revised January 9, 2020; accepted February 9, 2020. Date of publication February 19, 2020; date of current version March 17, 2020. This work was supported in part by the National Natural Science Foundation of China under Grants 61871080, 61771109, and 61701093, in part by Changjiang Scholar Program, in part by the 111 Project B17008, in part by Science & Technology Department of Sichuan Province Miaozi Project 2019JDRC0061, and in part by the GF Science and Technology Special Innovation Zone Project. (Corresponding author: Guolong Cui.)

The authors are with the School of Information and Communication Engineering, University of Electronic Science and Technology of China, Chengdu 611731, China (e-mail: lsl@std.uestc.edu.cn; cuiguolong@uestc.edu.cn; ssguo@uestc.edu.cn; jiachao@uestc.edu.cn; ljkong@uestc.edu.cn; yangxiaobo@uestc.edu.cn).

Digital Object Identifier 10.1109/JSTARS.2020.2974529

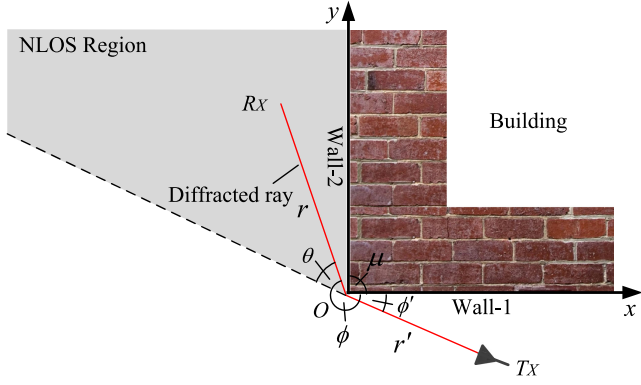


Fig. 1. EM diffraction propagation geometry model around building corner.

consider the problem of detecting and locating a moving target behind a corner exploiting reflected multipath returns [20]–[22]. Note that the detection problem of NLOS target aforementioned mainly rely on the EM wave reflection in corridors environment.

Different from those multipath scenarios aforementioned, we consider a single rectangular building corner scenario where only EM wave diffraction can be occurred, in which the preliminary research results have been reported in [23]. In this article, the deep analysis and results are presented to characterize the diffraction propagation in a single rectangular building corner scenario. First, two EM wave diffraction propagation paths are analyzed. Therein, one is the feasibility model of EM diffraction propagation without target and the antenna splitting, another is the diffraction echo model with the target and the transmitting and receiving antennas in the same position. The model-based diffraction of a single rectangular building corner is verified by simulation and real data experiment. Then, a target location algorithm is proposed based on the diffraction echo models for behind the corner environment. Finally, the feasibility of using diffraction to locate target behind the corner is verified by simulation and real data.

The rest of this article is organized as follows. In Section II, the EM diffraction propagation models around the building corner are introduced. Section III presents an application of EM diffraction propagation. Section IV concludes this article.

## II. EM DIFFRACTION PROPAGATION MODEL AROUND BUILDING CORNER

### A. NLOS Propagation Model

We consider a single building corner scenario, as shown in Fig. 1. Specifically, the corner structure is composed of wall-1 and wall-2. The origin of coordinates is marked as  $O = [x_O, y_O]^T$ . A transmitter  $Tx$  is located behind one side of the corner with the coordinates vector  $Tx = [x_T, y_T]^T$ . A receiver  $Rx$  is placed at the other side of the corner with the coordinates vector  $Rx = [x_R, y_R]^T$ . Due to the obstruction of the wall corner, the EM wave signal transmitted by  $Tx$  cannot reach the  $Rx$  directly. The NLOS region of interest is marked in Fig. 1 (shadow region). For any point  $(x_R, y_R)$  in the NLOS

region, the following relations are satisfied:

$$(x_R, y_R)^T \in \begin{cases} x_R < x_O, \\ y_R > y_O - \frac{(y_T - y_O)(x_R + x_O)}{x_T - x_O}. \end{cases} \quad (1)$$

Although the EM wave cannot propagate along LOS path to the NLOS region, it can propagate to the receiving antenna  $Rx$  by corner edge diffraction along the path  $Tx \rightarrow O \rightarrow Rx$ , as shown in Fig. 1.

In order to verify that EM wave can propagate from  $Tx$  to  $Rx$  by diffraction path in the single building corner scenario, an EM simulation experiment is conducted. The simulation is completed with XFDTD software, which is based on the finite-difference time-domain solver [24]. We consider a  $10 \text{ m} \times 10 \text{ m}$  building corner scenario, in which the transmitting antenna  $Tx$  is located at  $(1.0 \text{ m}, -1.0 \text{ m})$  and the receiving antenna  $Rx$  is located at  $(-1.0 \text{ m}, 3.0 \text{ m})$ . The relative dielectric constant of the building is 6 and the conductivity is  $0.05 \text{ S/m}$ . The transmitted signal is stepped-frequency continuous wave [25] with the frequency starting from  $1.0$  to  $2.0 \text{ GHz}$  and the frequency step is  $2.0 \text{ MHz}$ .

In Fig. 2, the EM field intensities at four different moments are given. The transmitted signal is first emitted from the transmitter in the form of a spherical wave, as shown in Fig. 2(a) (moment-1). Then, the EM wave will reflect at the wall-1 surface to form the wall reflection wave ① and diffracts at the corner to form the diffraction wave ②, as shown in Fig. 2(b) (moment-2). Finally, the EM wave passes around corner  $O$  via diffraction to reach the receiver, as shown in Fig. 2(c) and 2(d) (moment-3 and moment-4). In Fig. 3, we give the time-domain signal received by  $Rx$ . According to the layout of the scenario and the diffraction propagation path of the EM wave, the physical length of the diffraction path can be expressed as

$$l_{\text{diff}} = \sqrt{(x_T - x_O)^2 + (y_T - y_O)^2} + \sqrt{(x_O - x_R)^2 + (y_O - y_R)^2}. \quad (2)$$

Based on EM simulation parameters,  $l_{\text{diff}} = 4.58 \text{ m}$ .

From the above results, it can be seen that the diffraction signal can indeed be propagated to NLOS region by corner edge diffraction.

In order to better describe the law of EM wave diffraction, uniform geometrical theory of diffraction (UTD) is introduced in this article [26], [27]. According to the UTD, the diffracted field in NLOS region can be given by

$$\mathbf{E}_d = \mathbf{E}_i(O) A_d(r) D(\phi, \phi') e^{-jkr} \quad (3)$$

where  $k = 2\pi/\lambda$  represents the propagation constant,  $\lambda$  denotes the wavelength,  $A_d(r)$  is the spreading factor ensuring the proper attenuation rate and can be expressed as

$$A_d(r) = \sqrt{\frac{r'}{r(r+r')}} \quad (4)$$

where  $r'$  and  $r$  are the distance values from the corner edge to the transmitter  $Tx$  and receiver  $Rx$ , respectively.  $\mathbf{E}_i(O)$  is the

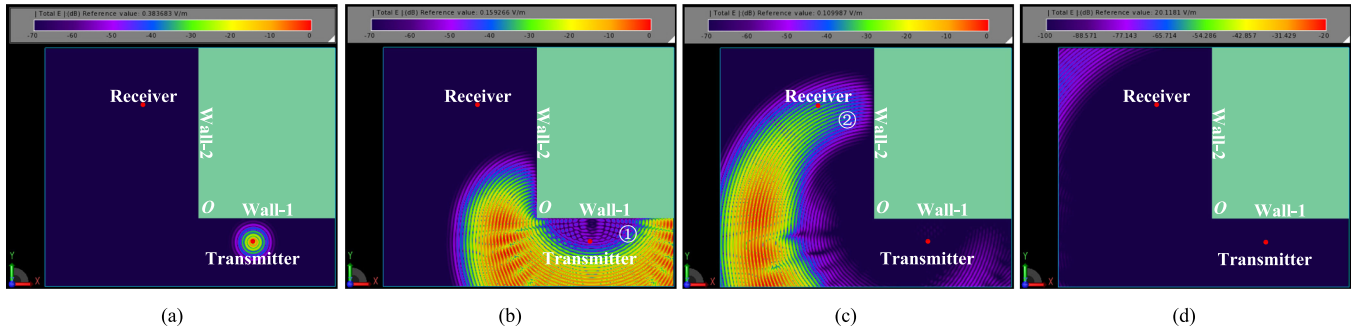


Fig. 2. Propagation process of EM wave around the single building corner without target (view from +Z). (a) Moment-1. (b) Moment-2. (c) Moment-3. (d) Moment-4.

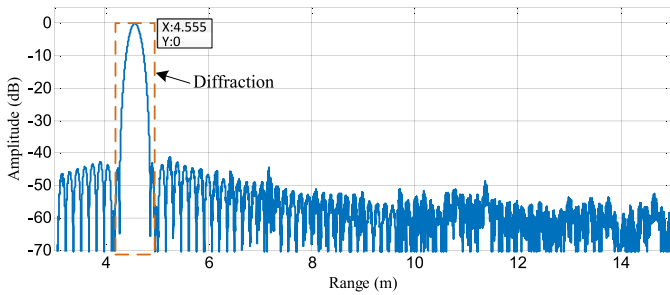


Fig. 3. Received signal of Rx behind the building corner corresponding to results of Fig. 2.

incident field on the corner edge, which can be denoted by

$$\mathbf{E}_i(O) = \mathbf{E}_O \frac{e^{-jkr'}}{r'} \quad (5)$$

Specifically, the product of  $A_d$ ,  $\mathbf{E}_i(O)$  and  $e^{-jkr}$  is invariant. Assume that the E-field parallel to the building corner edge, then the diffraction coefficient  $D(\phi, \phi')$  can be calculated as

$$D(\phi, \phi') = \frac{-1}{2\kappa\sqrt{2\pi k\sin\mu}} \left[ \cot\left(\frac{\pi + (\phi - \phi')}{2\kappa}\right) + \cot\left(\frac{\pi + (\phi + \phi')}{2\kappa}\right) - \cot\left(\frac{\pi - (\phi - \phi')}{2\kappa}\right) - \cot\left(\frac{\pi - (\phi + \phi')}{2\kappa}\right) \right] \quad (6)$$

where  $\phi$  denotes diffraction angle,  $\phi'$  represents the included angle between the line connected  $Tx$  and the corner  $O$  and the surface of wall-1, and  $\mu$  is the interior angle of the corner edge. The exterior angle of the corner edge is  $\kappa\pi$ ,  $\kappa \in [0, 2]$ . Since the right angle edge corner is considered in this article, it is readily derived that the values of  $\mu$  and  $n$  are  $90^\circ$  and  $3/2$ , respectively.

According to the above analysis, we can see that the distribution of diffraction field intensity is mainly related to the diffraction angle  $\phi$  and propagation distance  $r$  when the coordinates of the radar and the wall corner are known *a priori*. To conduct a quantitative analysis, a numerical simulation based on MATLAB

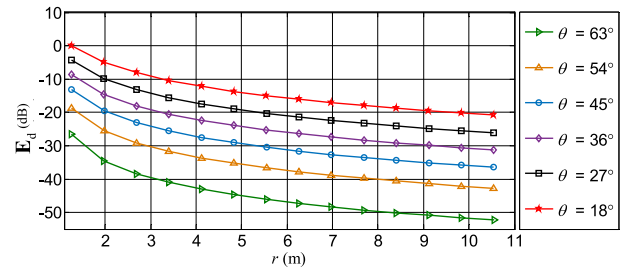


Fig. 4. Relation curves of EM wave diffraction field intensity.

is implemented. We first determine that  $\phi'$  corresponding to the receiving antenna  $Rx$  equals  $21.8^\circ$  ( $\phi' = \arctan(y_T/x_T)$ ), and  $\phi \in [180^\circ, 270^\circ]$ . To simplify the analysis, we map  $\phi$  to  $[0^\circ, 90^\circ]$  and use  $\theta$  to represent them ( $\theta = \pi + \phi' - \phi$ , see Fig. 1). Furthermore, six different values of  $\theta$  ( $18^\circ, 27^\circ, 36^\circ, 45^\circ, 54^\circ, 63^\circ$ ) are considered when the transmitting antenna  $Tx$  is located at the same position. The received signal amplitudes of these angles at different distances from the corner  $O$  are obtained.

Fig. 4 shows the corresponding curves of diffraction field intensity  $\mathbf{E}_d$  with the diffraction angle  $\theta$  and distance  $r$ . Specifically, when the value of  $r$  is fixed, the diffraction intensity received by  $Rx$  at six different locations satisfy the following relationships:  $\mathbf{E}_{d,\theta=18^\circ} > \mathbf{E}_{d,\theta=27^\circ} > \mathbf{E}_{d,\theta=36^\circ} > \mathbf{E}_{d,\theta=45^\circ} > \mathbf{E}_{d,\theta=54^\circ} > \mathbf{E}_{d,\theta=63^\circ}$ , that is, the larger the diffraction angle, the worse the diffraction effect. Similarly, when the value of  $\theta$  is fixed, we can obtain another conclusion, namely, the larger the distance between the target and the corner  $O$ , the weaker the intensity of the received diffraction signal.

According to (3), the diffracted field  $\mathbf{E}_d$  and the diffraction propagation area are determined by the diffraction angle  $\phi$  and range  $r$ . In order to explain the relationship between the diffraction angle and range and the diffraction propagation area intuitively, the simulation of the diffraction path loss coverage is developed in a single building corner scenario. The simulation parameters are consistent with the simulation in Fig. 2. Cover simulation is carried out for 22 500 receiver positions at  $x = 0.067 \text{ m}, \dots, 10 \text{ m}$  and  $y = 0.067 \text{ m}, \dots, 10 \text{ m}$  with a step size of  $\Delta x = \Delta y = 0.067 \text{ m}$ . The transmit antenna  $Tx$  and corner  $O$  are located at  $(9 \text{ m}, 1 \text{ m})$  and  $(7 \text{ m}, 2 \text{ m})$ , respectively.



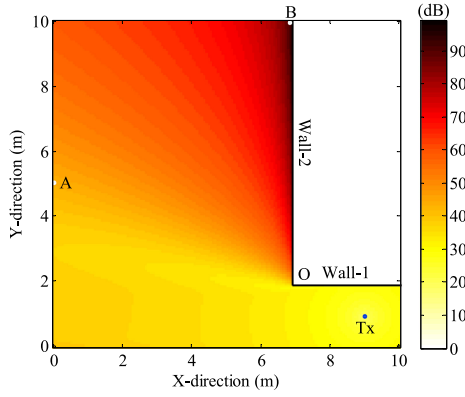


Fig. 5. Coverage map for path loss of single building corner scenario diffraction propagation.

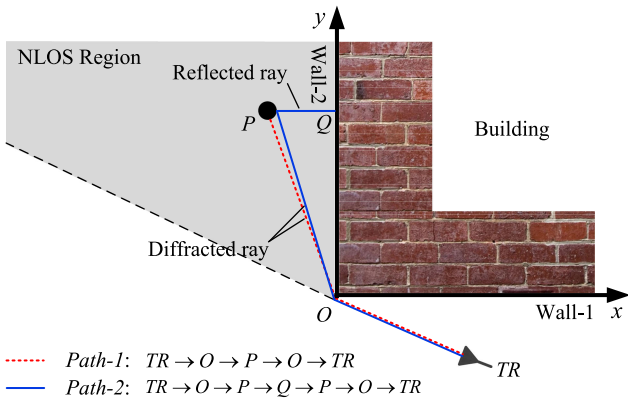


Fig. 6. EM diffraction propagation geometry model in the present of target around building corner.

Fig. 5 shows the result of the path loss for the single building corner scenario. The maximum path loss under LOS conditions is 39 dB, as shown in white A point in Fig. 5. For NLOS area, the signal can completely cover the NLOS area with a different path loss. It can be seen that the color map deepens gradually with the increase of diffraction angle and range, that is, the diffraction path loss increases gradually with the increase of diffraction angle and range. The maximum loss is 93 dB, as shown in white B point in Fig. 5.

### B. NLOS Propagation Model in the Present of Target

In this section, we consider the scenario where there is a target in the same building structure as NLOS propagation model in Section-II, as shown in Fig. 6. The coordinates of the target are  $P = [x_P, y_P]^T$  in the NLOS region. Unlike the scenario of NLOS propagation model in Section-II, the transmitter and the receiver are placed in the same place with the coordinates  $TR = [x_{TR}, y_{TR}]^T$  in this section.

Based on the characteristics of EM wave diffraction, we know that the EM wave can be propagated to the target position by corner edge diffraction. When there is a target in the scene, the EM wave will reflect on the surface of the target when it propagates by the corner diffraction to the NLOS region. A part of the reflected EM wave will be diffracted back to

the receiving antenna  $TR$ . Thus, the propagation path of EM wave in this process is  $TR \rightarrow O \rightarrow P \rightarrow O \rightarrow TR$ , as shown in Fig. 6. In addition, the EM wave reflected from the target surface propagates to the surface of wall-2 and reflects again. Suppose that the reflection point of EM wave on the surface of wall-2 is denoted as  $Q = [x_Q, y_Q]^T$ . The corresponding propagation path is  $TR \rightarrow O \rightarrow P \rightarrow Q \rightarrow P \rightarrow O \rightarrow TR$ , as shown in Fig. 6. Hence, the echoes of these two propagation paths are included in the returns. In order to verify the existence of these paths, the following several EM simulation and real data collection experiments are carried out.

1) *EM Simulation Analysis*: In XFDTD-based simulation, the target is set as a perfect electric conductor (PEC) cylinder with radius of 0.2 m, and the coordinates are  $(-1.75 \text{ m}, 3.25 \text{ m})$ . The relative dielectric constant of the target is 55 and the conductivity is 1.05 S/m. The radar system is located at  $(1.0 \text{ m}, -1.0 \text{ m})$  to detect the concealed target. Other parameters including the wall, and the transmitted signal are consistent with those of the simulation of NLOS propagation model in Section-II.

Fig. 7 shows that the EM field distribution of eight different moments for the propagation progress of EM wave. First, the EM wave is transmitted from  $TR$  and can be seen as a spherical EM wave in Fig. 7(a). Fig. 7(b) shows that the EM wave is reflected at the surface of wall-1 to form echo ①. In Fig. 7(b) and (c), EM wave diffraction occurs at the corner  $O$  to form diffraction EM wave ②, and the EM wave continue to propagate forward. Then, the EM wave ② reflects on the target surface to form target reflection wave ③ in Fig. 7(d). Subsequently, the target reflection wave ③ forms diffraction EM wave ⑤ by diffracting again on corner  $O$ , and returns to the location ⑤ of the radar, as shown in Fig. 7(e) and (f). Note that there is also echo ④, that is, the wall-2 surface reflected wave, as shown in Fig. 7(e). Then, the EM wave ④ is reflected again on the target surface to form the wave ⑥, as shown in Fig. 7(f). Finally, the EM wave ⑥ propagates back to the radar by corner diffraction, as shown in Fig. 7(g) and (h). Due to the strong attenuation caused by multiple reflections between the target and the surface of wall-2, the echo ⑧ and ⑨ can be ignored.

Furthermore, the range profile results in the above simulation experiment are given in Fig. 8. Specifically, Fig. 8(a) shows the original echo signal. Note that there is a peak with the strongest amplitude, namely, the echo peak related to the antenna coupling. Because the transmitting antenna and the receiving antenna are located in the same position, the peak of antenna coupling appears at zero.

In order to detect the weak target signals that are overlaid by strong antenna coupling and reflections from walls or other dominant static objects in indoor scenarios, the moving target indication (MTI) method is employed. Two pulse subtraction [28] and average subtraction [29] are commonly used in MTI. In this article, two-pulse subtraction method is employed. Suppose that  $s^{(m)}$  and  $s^{(m+1)}$  denote the corresponding original echo range profile with respect to the  $m$ th and  $m+1$ th period, respectively,  $m = 1, 2, \dots, M$ . Then, the operation of two-pulse subtraction can be expressed as

$$\hat{s}^{(m)} = s^{(m)} - s^{(m+1)} \quad (7)$$

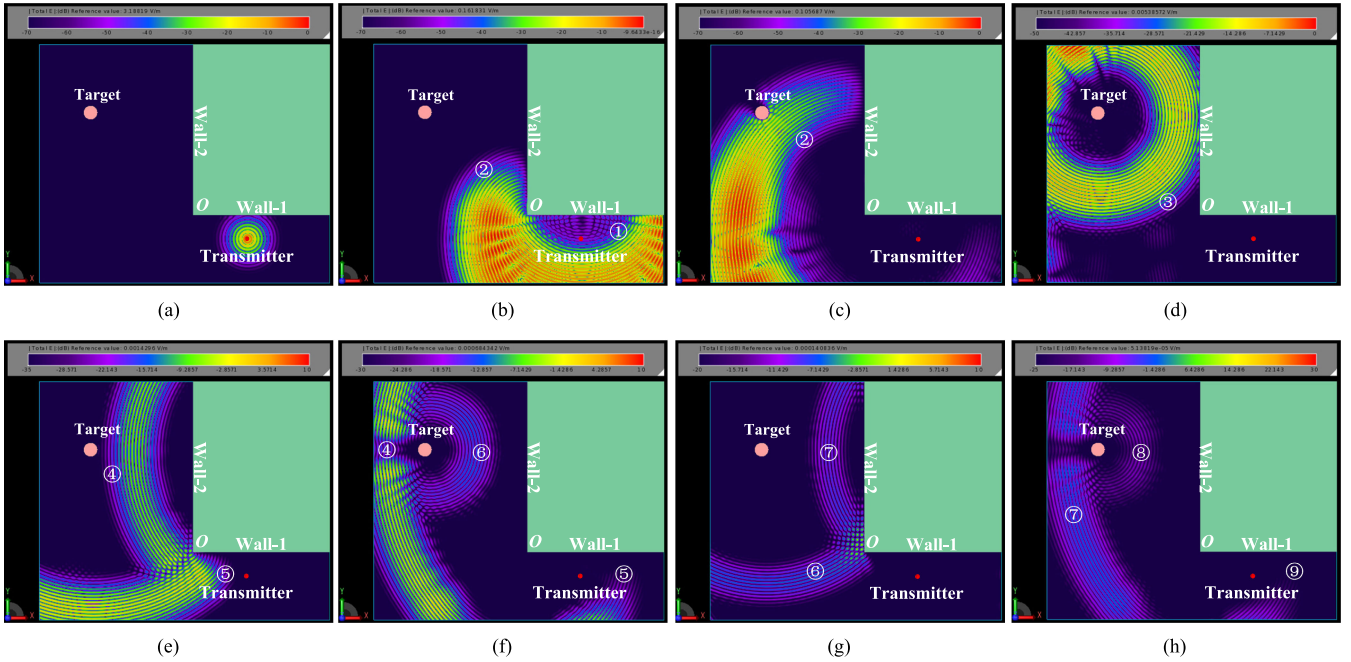


Fig. 7. Propagation process of EM wave around the single building corner in the presence of target (view from +Z), (a) moment-1, (b) moment-2, (c) moment-3, (d) moment-4, (e) moment-5, (f) moment-6, (g) moment-7, and (h) moment-8.

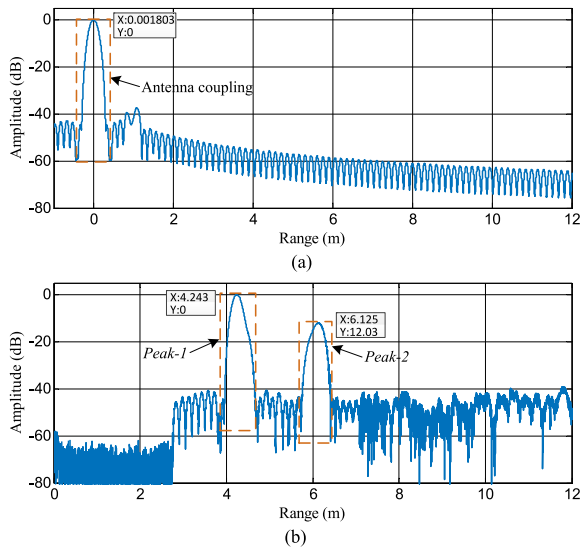


Fig. 8. Range profile of the simulation results with respect to Fig. 7. (a) Original echo signal. (b) Target echoes signal after two-pulse subtraction.

where  $\hat{s}^{(m)}$  represents the range profile after two-pulse subtraction.

The target range profile after two-pulse subtraction is shown in Fig. 8(b). Note that there are two peaks with strong amplitudes, in which the strongest peak (Peak-1) is associated with wave ⑤ in Fig. 7(e), while the secondary strength peak (Peak-2) corresponds to the wave ⑥ in Fig. 7(g).

In this article, we define the propagation paths of these two peaks as *Path-1* and *Path-2*, respectively. According to the propagation characteristics of EM wave, we know that the

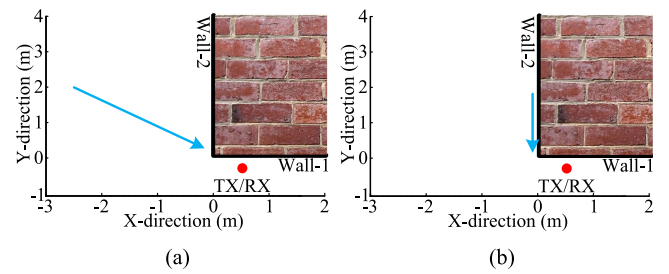


Fig. 9. Plane of simulation scene with different target moving states. (a) Case-1: target moves along a straight line gradually close to the corner. (b) Case-2: target moves along straight line parallel to the surface of wall-2 and gradually closes to the corner.

propagation path lengths of *Path-1* and *Path-2* satisfy the following relationship:

$$|l_{\text{Path-1}} - l_{\text{Path-2}}| = \|\text{PQ}\| \quad (8)$$

where  $|\cdot|$  denotes absolute value symbol,  $\|\cdot\|$  represents Euclidean distance, and  $l_{\text{Path-1}}$  and  $l_{\text{Path-2}}$  represent lengths of *Path-1* and *Path-2*, respectively.

In order to further verify the existence of the above EM wave diffraction propagation paths, an EM simulation considering multiple target test points is conducted based on the same simulation scenario with NLOS propagation model in the presence of target in Section II. The acquisition of EM simulation data of moving target is realized by gprMax software with graphics processing unit multithreaded parallel calculation [30]. In this simulation, we consider two different moving cases of the target. In case-1, the target moves from  $(-2.0 \text{ m}, 2.0 \text{ m})$  to  $(-0.4 \text{ m}, 0.4 \text{ m})$  along a straight line, as shown in Fig. 9(a). While, in case-2, the target moves from  $(-0.4 \text{ m}, 1.8 \text{ m})$  to  $(-0.4 \text{ m}, 0 \text{ m})$ ,

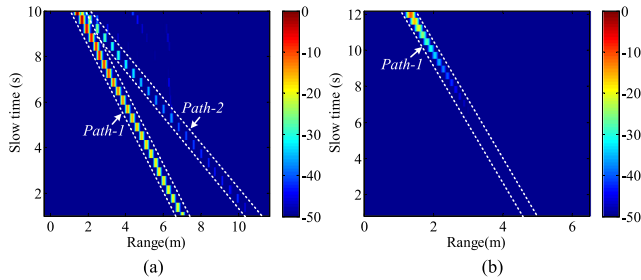


Fig. 10. Range profile plane with respect to simulation data. (a) Range profile plane of case-1. (b) Range profile plane of case-2.

TABLE I  
KEY PARAMETERS OF UWB RADAR

Parameters	Value
Starting frequency	1.6 GHz
Ending frequency	2.2 GHz
Bandwidth	600 MHz
Number of steps	301
Frequency step	2 MHz
Radiation power	18 dBm

0.4 m) along straight line parallel to the surface of wall-2, what is closed to the wall, as shown in Fig. 9(b).

Fig. 10(a) shows the moving target range profile plane of case-1. Note that there are two different range trajectories, which correspond to *Path-1* and *Path-2*, respectively (see the dotted line covered in Fig. 10). It is clear that the peak intensity of *Path-1* and *Path-2* decreases gradually when the target approaches the corner. Moreover, we can see that the distance between the two range trajectories along the *X*-axis decreases gradually with time. Similarly, Fig. 10(b) shows the moving target range profile plane of case-2. Due to the target moves along straight line parallel to the surface of wall-2 ( $l_{\text{Path-2}} = 0$  m). Thus, there is only one range trajectory, which corresponds to *Path-1*. In particular, the effect of EM diffraction is very poor for the initial target position in case-2. Hence, the target echo amplitude intensity is high only near the corner.

2) *Real Data Experiment Analysis*: To further verify the existence of the EM wave propagation phenomena aforementioned in real environment, real data are collected by using the stepped frequency continuous wave L-band radar system with one transmitting antenna (*Tx*) and one receiving antenna (*Rx*). Both antennas are vertically polarized. The distance between *Tx* and *Rx* is 0.075 m. The center coordinates of ultra-wideband (UWB) radar system are  $(-0.45$  m,  $0.35$  m). *Tx* antenna and *Rx* antenna are placed at 1.2 m high from the ground, and the antenna array is directed toward the diffracting corner. Specifically, the detailed parameters of the radar system are listed in Table I. The pictures of the measurement environment and the UWB radar are shown in Fig. 11. Note that the location of radar is chosen because it is isolated with no nearby buildings or automobile traffic to cause backscattered energy.

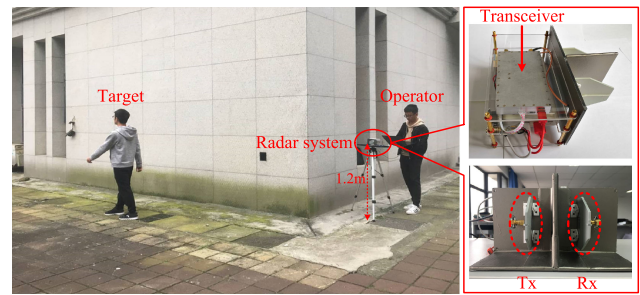


Fig. 11. Pictures of the experimental scenario and the SISO UWB radar device.

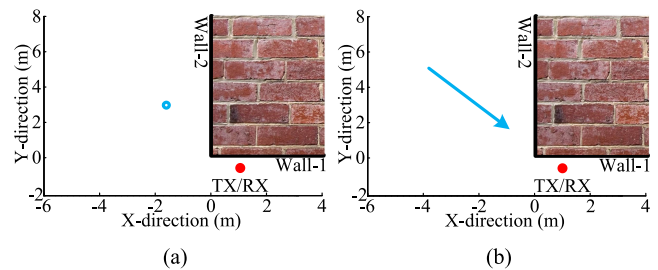


Fig. 12. Scene plan of EM simulation and experiment: (a) micro target and (b) moving target.

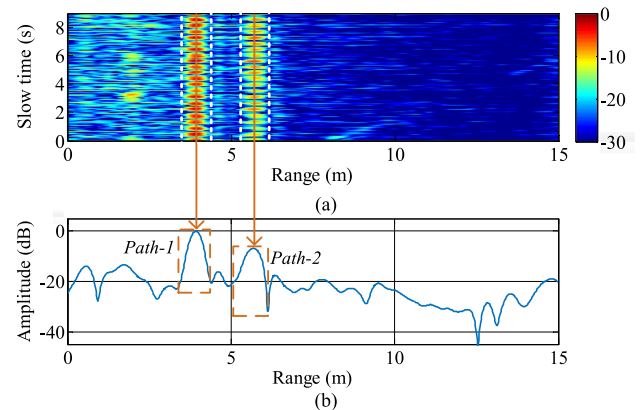


Fig. 13. Real data results of micromotion target. (a) Range profile plane with respect to 600 periods of real data (dB). (b) Echo signal of the 120th period.

Two experiments considering different target move conditions are conducted, as shown in Fig. 12. In the first experiment, the person stands at the position  $(-1.8$  m,  $3.0$  m) at first. Then, he is swaying back and forth with a small range during the data collection [see micromotion target in Fig. 12(a)]. A total of 600 periods of data are collected during the experiment. The corresponding micromotion target range profile plane is obtained after background subtraction, as shown in Fig. 13(a). Note that the two strong range trajectories of the micromotion target can be seen clearly, one of which at 3.9 m (with respect to *Path-1*) and another at 5.7 m (with respect to *Path-2*). To prove the above statement intuitively, we give the range profile result of the 120th period in Fig. 13(b). According to Fig. 13(a) and Fig. (b), we know that the target distance fluctuates around a small range and the peak intensity of *Path-2* is weaker than



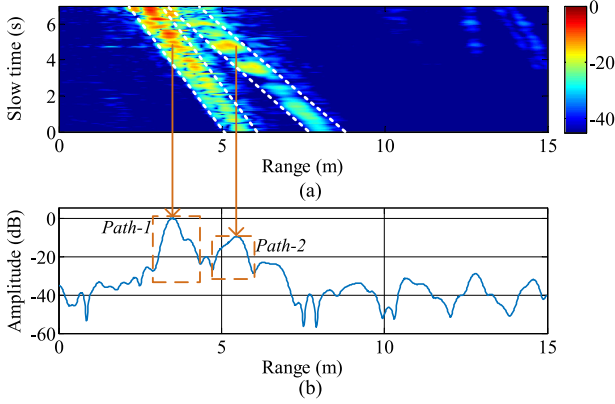


Fig. 14. Real data result of moving target. (a) Range profile plane with respect to 500 periods of real data (dB). (b) Echo signal of the 350th period.

that of *Path-1*. Furthermore, it is readily found that the peak amplitude corresponding to *Path-1* and *Path-2* is obviously higher than the clutter signal. It is worth mentioning that we can observe some range trajectories other than the target echoes in the range profile plane, mainly because of the micromotion of the experimental operator. Considering the weak amplitude of these echoes, there is no essential influence on target echoes detection.

Different from the first experiment, the human walks along straight route from  $(-3.5 \text{ m}, 5.2 \text{ m})$  to  $(-1.0 \text{ m}, 2.0 \text{ m})$  in the second experiment [see Fig. 12(b)]. A total of 500 periods of data are collected in this experiment. Similarly, the MTI technology is employed to suppress background clutter. According to the range trajectory shown in Fig. 14(a), there are two inclined range profile trajectories, the strongest one is with respect to *Path-1* and the second strongest one is related to *Path-2*. The range profile trajectory corresponds to *Path-1* ranges from 2.78 to 5.62 m, while that of *path-2* ranges from 4.22 to 8.13 m. To prove the above statement intuitively, we give the range profile result of 350th period in Fig. 14(b). Similarly, there are also two peaks with high amplitudes corresponding to *Path-1* and *Path-2*, respectively. The characteristic of range profile trajectory of moving target is consistent with the simulation results of Fig. 10(a). Due to the expansion characteristics and the body swing of human targets, it is clear that the range profile trajectories in Fig. 14(a) has a larger expansion than micromotion target in Fig. 13(a).

In this section, the correctness of the EM wave diffraction propagation model in single building corner scene has been verified by simulation and real data experiments. In the next section, we will introduce one of the application of these two EM wave propagation model above.

### III. APPLICATION OF EM DIFFRACTION

In this section, we will introduce one application of these two EM wave diffraction propagation paths mentioned in Section-II. Specifically, an NLOS target localization approach is proposed for single corner scenario by single-input single-output (SISO) UWB radar.

#### A. Signal Model

Let  $z(t)$  denote the transmitted signal, which has the following form:

$$z(t) = \sum_{n=0}^{N-1} e^{j2\pi(f_0+n\Delta f)t} \text{rect}\left(\frac{t-nT_0-T_0/2}{T_0}\right) \quad (9)$$

where  $T_0$  denotes the pulse repetition interval,  $K$  is the number of frequencies,  $f_0$  represents the starting frequency, and  $\Delta f$  is the frequency step.  $\text{rect}(x)$  denotes the rectangle function and can be expressed as

$$\text{rect}(x) = \begin{cases} 1, & |x| \leq \frac{1}{2} \\ 0, & \text{otherwise.} \end{cases} \quad (10)$$

For the receiver, the  $m$ th period echo  $s_0^{(m)}(t)$  can be denoted by

$$s_0^{(m)}(t) = \sigma_i z\left(t - \tau_{\text{path-}i}^{(m)}\right) + \xi(t) + \omega(t) + \varphi(t), \quad i = 1, 2 \quad (11)$$

where  $\sigma_1$  and  $\sigma_2$  are the complex attenuation coefficients of two strong different round-trip paths,  $\xi(t)$  represents echoes from other complex propagation paths, such as high-order reflection echo, and  $\omega(t)$  indicates the received direct-coupled signal by the receiver from the transmitter and summarizes the clutters caused by the reflections from walls, which is much stronger than the signal reflected from targets.  $\varphi(t)$  denotes the noises and interferences in the environment.  $\tau_{\text{path-}1}^{(m)}$  and  $\tau_{\text{path-}2}^{(m)}$  are the round-trip time delays related to *path-1* and *path-2* for the  $m$ th period of transmitted signal and can be expressed as

$$\begin{cases} \tau_{\text{path-}1}^{(m)} = \frac{l_{\text{path-}1}^{(m)}}{c} \\ \tau_{\text{path-}2}^{(m)} = \frac{l_{\text{path-}2}^{(m)}}{c} \end{cases} \quad (12)$$

where  $l_{\text{path-}1}^{(m)}$  and  $l_{\text{path-}2}^{(m)}$  represent path lengths of *path-1* and *path-2*, respectively, and  $c$  denotes the propagation velocity of EM wave.

#### B. Description of Target Location Algorithm

Note that the echoes scattered by hidden target will be revealed after the two-pulse subtraction algorithm. However, the ranges with to *path-1* and *path-2* should be estimated to obtain the location of the hidden target in NLOS area. Thus, in the following, we will give the detailed target location algorithm.

First, in order to accurately extract the peaks correspond to *path-1* and *path-2*, the median filtering is adopted in this article. For the range profile of the  $m$ th period, the number of range cells is set as  $I_1$ . Then, by using the sliding window method, we can obtain  $I_2$  range cell windows with equal length  $I_3 = 2L + 1$  ( $I_1 > I_3$ ). For a common window, let the  $i$ th moment range cell sequence be denoted as  $\hat{s}^{(m)}(i-L), \dots, \hat{s}^{(m)}(i), \dots, \hat{s}^{(m)}(i+L)$ . Then, the process of median

filtering can be denoted as

$$\begin{aligned} & \widehat{\mathbf{s}}_1^{(m)}(i) \\ &= \text{med} \left\{ \widehat{\mathbf{s}}^{(m)}(i-L), \dots, \widehat{\mathbf{s}}^{(m)}(i), \dots, \widehat{\mathbf{s}}^{(m)}(i+L) \right\} \end{aligned} \quad (13)$$

where  $\widehat{\mathbf{s}}_1^{(m)}$  denotes the signals after median filtering.  $\text{med}\{\cdot\}$  indicates that all the range cells in the window are arranged in ascending order, and then takes the median operation.

Based on the data after median filtering, cell averaging constant false alarm rate (CA-CFAR) technique is utilized to extract the range information of *path-1* and *path-2* from the range profiles [31]. The adaptive threshold of CA-CFAR is given by

$$\widehat{T}_s(i) = \left( P_{\text{FA}}^{-1/N} - 1 \right) \sum_{i=1}^N \widehat{\mathbf{s}}_1^{(m)}(i) \quad (14)$$

where  $N$  is the number of reference cells,  $\widehat{\mathbf{s}}_1^{(m)}(i)$  represents the  $i$ th reference cell, and  $P_{\text{FA}}$  denotes the probability of false alarm. The threshold detection process is as follows:

$$\widehat{\mathbf{s}}_1^{(m)}(i) = \begin{cases} 1, & \widehat{\mathbf{s}}_1^{(m)}(i) \geq \widehat{T}_s(i) \\ 0, & \widehat{\mathbf{s}}_1^{(m)}(i) < \widehat{T}_s(i). \end{cases} \quad (15)$$

Repeating the above operations for the whole range cells, the path propagation time delays  $\tau_{\text{path-1}}^{(m)}$  and  $\tau_{\text{path-2}}^{(m)}$  are obtained. Furthermore, the propagation distance difference  $\Delta l$  between the *path-1* and the *path-2* is given by

$$\Delta l^{(m)} = \left| l_{\text{path-2}}^{(m)} - l_{\text{path-1}}^{(m)} \right|. \quad (16)$$

Meanwhile, with the known building layout and radar position, the distance between the radar  $R$  and the corner  $O$  can be computed as

$$l_{RO} = \sqrt{(x_R - x_O)^2 + (y_R - y_O)^2}. \quad (17)$$

Then, the coordinates of the hidden target  $P$  in the  $m$ th data period can be calculated as

$$\begin{cases} x_P^{(m)} = x_O - \frac{\Delta l^{(m)}}{2} \\ y_P^{(m)} = y_O + \sqrt{\left( \frac{l_{\text{path-1}}^{(m)}}{2} - l_{RO} \right)^2 - \left( \frac{\Delta l^{(m)}}{2} \right)^2}. \end{cases} \quad (18)$$

Repeat the steps above, and the target positions for these data can be obtained. Due to the existence of noises and clutters, the false target localization results may be computed. To tackle this problem, several strategies are used to eliminate the false targets. Based on the known of building layout, the LOS area or the building area can be expressed as

$$\begin{aligned} & \left\{ (x_P^{(m)}, y_P^{(m)}) : \geq x_O \right\} \cap \\ & \left\{ (x_P^{(m)}, y_P^{(m)}) : y_P^{(m)} \leq y_O - \frac{(y_{TR} - y_O)(x_P^{(m)} + x_O)}{x_{TR} - x_O} \right\}. \end{aligned} \quad (19)$$

Hence, the false target positions located at these area can be eliminated directly.

According to the feature that the true target is still located in the NLOS area, we can use the  $\alpha$ - $\beta$  filtering to obtain smooth target trajectory [32]. Suppose that  $M$  periods of data have been collected, the  $M$  localization results are expressed as  $\mathbf{X}(M)$ ,  $m = 1, 2, \dots, M$ . In the case of a single target, the prediction state of target is expressed as

$$\widehat{\mathbf{X}}(m+1|m) = \mathbf{F}(m)\widehat{\mathbf{X}}(m|m) \quad (20)$$

where  $\widehat{\mathbf{X}}(m|m)$  is the state estimate value of the track at the  $m$ th period,  $\widehat{\mathbf{X}}(m+1|m)$  denotes the state value of the  $(m+1)$ th period estimated in the  $m$ th period, and  $\mathbf{F}$  indicates the transition matrix.

Based on the estimated value above, the state update equation can be expressed as

$$\widehat{\mathbf{X}}(m+1|m+1) = \widehat{\mathbf{X}}(m+1|m) + \mathbf{K}(m+1)\mathbf{v}(m+1) \quad (21)$$

where  $\mathbf{K}$  denotes gain. For an update time  $T_U$ , the matrix  $\mathbf{K}$  is expressed as

$$\mathbf{K} = [\alpha \beta / T_U]^T. \quad (22)$$

In (23), we give the innovation equation  $\mathbf{v}(m+1)$

$$\mathbf{v}(m+1) = \mathbf{Z}(m+1) - \mathbf{H}(m+1)\widehat{\mathbf{X}}(m+1|m) \quad (23)$$

where  $\mathbf{H}$  is an observation matrix, and  $\mathbf{Z}(m+1)$  indicates the target position of the  $(m+1)$ th period updated by (21).

### C. EM Simulation and Real Data Experiment

In this section, several EM simulation and experimental results are provided to validate the proposed hidden target localization approach.

1) *EM Simulation*: The size of simulation zone is 10 m  $\times$  10 m, as shown in Fig. 12. All of the simulation data are also collected by using gprMax software. In particular, the simulation parameters are the same as those of NLOS propagation model in the presence of target in Section II. The center of radar system is located at (1.0 m, -0.5 m). We consider two different target moving states in the different simulation. Note that the target is located in the NLOS area of the radar in both different simulation.

In the first simulation, the micromotion target stands at the (-1.8 m, 3.0 m) with swaying back and forth with a small range, as shown in Fig. 12(a). Based on the range profiles, the two-dimensional (2-D) position of the target can be calculated by using the proposed algorithm. The locations of the micromotion target are clearly presented in Fig. 15. The measured mean position of the target is (-1.64 m, 2.97 m), while the deviation between the initial position and the mean position is about 0.16 m. In order to verify the effectiveness of the proposed method more intuitively, the positioning error curve between the target estimated positions and the true target positions is given in Fig. 16(a). Therein, the abscissa of Fig. 16 denotes the period index of range profile while the ordinate represents the positioning error. According to the error curve, we can see that the maximum error between the estimated positions and



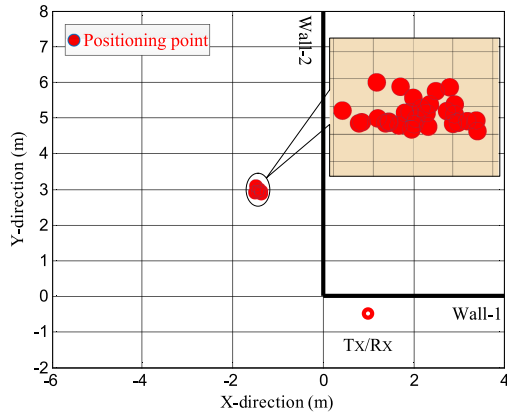


Fig. 15. Micromotion target localization results for the simulation data.

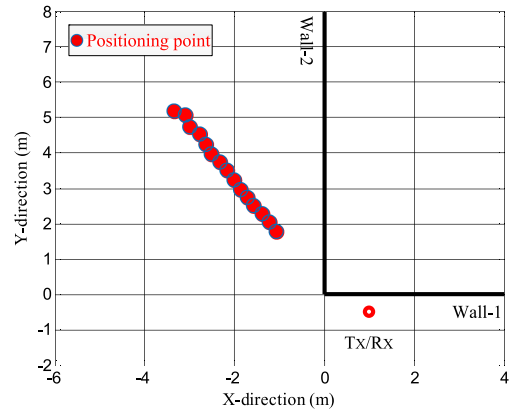


Fig. 17. Moving target localization results for the simulation data.

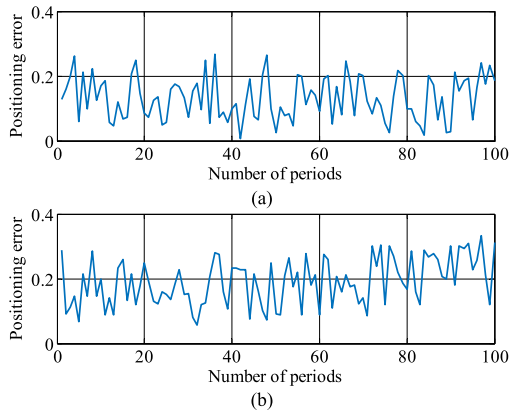


Fig. 16. Hidden target positioning error curve of simulation data. (a) Positioning error curve of micromotion target. (b) Positioning error curve of moving target.

the true positions of target is less than 0.28 m. Considering the radar resolution and the expansibility of human target, the above positioning errors are acceptable.

Next, we analyze the moving target positioning results for the second experiment. Specifically, the target moves along a straight route from  $(-3.4 \text{ m}, 5.2 \text{ m})$  to  $(-1.2 \text{ m}, 2.0 \text{ m})$  during the data collection, as shown in Fig. 12(b). By exploiting the proposed approach, the target estimated positions can be obtained, as shown in Fig. 17. It can be seen that the calculated target moving trajectory is located along the real motion route. A few target estimated positions are deviated from the real route in the end of the trajectory. For illustration, Fig. 16(b) gives the positioning error curve with respect to the moving target. Note that the location deviation is within the range of 0.04–0.32 m.

In order to quantitatively analyze the relationship between diffraction angle, range, and positional accuracy, several numerical simulations are carried out. As shown in Fig. 1, a case of the same diffraction range  $r = 5 \text{ m}$  is considered, where the diffraction angle  $\phi$  is set to  $\{215^\circ, \dots, 265^\circ\}$  with a step of  $\Delta\phi = 1^\circ$ . The curve of the diffraction angle and the positioning error is shown in Fig. 18(a), from which it can be seen that the positioning error of the target increases with the diffraction angle

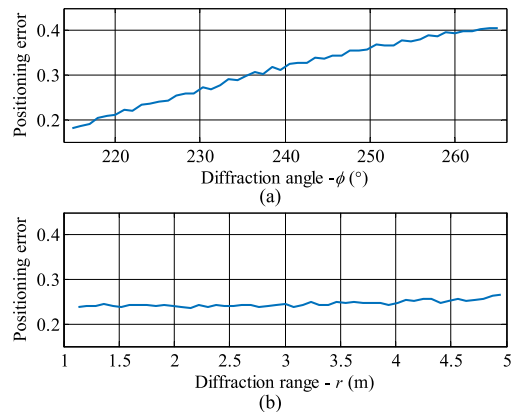


Fig. 18. Curve of the diffraction angle and range with the target positional accuracy. (a) Diffraction angle  $\phi$ . (b) Diffraction range  $r$ .

increases. The minimum and maximum positioning errors are 0.19 and 0.41 m, respectively.

The other case with the same diffraction angle  $\phi = 225^\circ$  is considered, where the diffraction range  $r$  is set to  $\{r = 1.13 \text{ m}, \dots, 4.95 \text{ m}\}$  with a step of  $\Delta r = 0.08 \text{ m}$ . The curve of diffraction range and positioning error is shown in Fig. 18(b), from which it can be seen that the positioning error of the target increases slowly with the diffraction range increases. The minimum and maximum positioning error are 0.26 and 0.23 m, respectively. The influence of diffraction angle on target positioning accuracy is greater than that of diffraction range. Specifically, when the diffraction angle  $\phi = 265^\circ$ , that is, the target is close to the surface of wall-2, the echo corresponding to *Path-1* and *Path-2* may overlap, resulting in the degradation of positioning performance.

According to the EM propagation process shown in Fig. 7, a round-trip reflection path between the target and the surface of wall-2 is observed. In the case of the single rectangular corner of the building, the reflection angle of the wall corresponding to the round-trip reflection path is a right angle. Moreover, the position and length of the reflection path are determined by the reflection angle of the target. Hence, to analyze the error from the reflection angle of the target, several EM propagation simulations are carried out with target is located at different positions,

TABLE II  
PROPAGATION PATH ERROR AND POSITIONING ERROR FOR DIFFERENT TARGET POSITION

Target Position	$P_1$	$P_2$	$P_3$	$P_4$	$P_5$	$P_6$	$P_7$	$P_8$	$P_9$	$P_{10}$
$\epsilon_{Path-1}$ (m)	0.1090	0.1105	0.1090	0.1091	0.1100	0.1090	0.1094	0.1103	0.1095	0.1103
$\epsilon_{Path-2}$ (m)	0.1855	0.2028	0.1902	0.1889	0.2019	0.1986	0.1936	0.1968	0.1915	0.1991
$\epsilon_P$ (m)	0.2722	0.2482	0.2653	0.2678	0.2481	0.2509	0.2607	0.2583	0.2644	0.2543

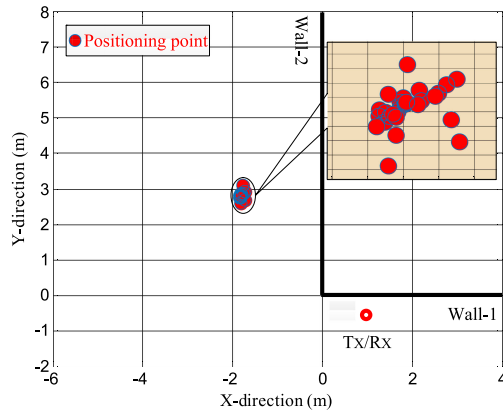


Fig. 19. Real data localization results of the micromotion target.

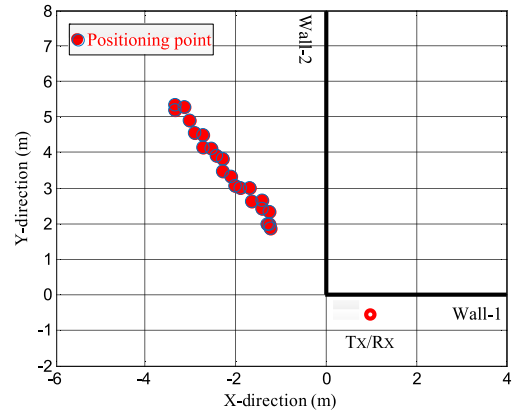


Fig. 20. Real data localization results of the moving target.

which are expressed as  $P_1, P_2, \dots, P_{10}$ . The errors  $\epsilon_{Path-1}$  and  $\epsilon_{Path-2}$  between the theoretical lengths and extracted locations of *Path-1* and *Path-2* are listed in Table II, respectively. The corresponding positioning errors  $\epsilon_P$  are also listed. According to Table II, the average errors of  $\bar{\epsilon}_{Path-1}$  and  $\bar{\epsilon}_{Path-2}$  are 0.1096 and 0.1949 m, respectively. Similarly, the average positioning errors  $\bar{\epsilon}_P$  is 0.2590 m.

In summary, the errors considered in this article are from diffraction angle, diffraction range, target reflection, and wall reflection, which are proved by numerical simulations. In practice, when considering the size of the target, the above errors will not have an essential impact on the target location results. The proposed algorithm can achieve good NLOS corner target positioning performance.

2) *Real Data Experiment*: To validate the proposed target localization algorithm experimentally, real data are collected by using the SISO UWB radar system. The geometric scene and experimental scenario have been described in Section II. Similarly, in order to ensure the validity of the data, the target sways back and forth with a small range or moves in the NLOS area of the radar in two different real data experiments.

First, we carry out an experiment considering the case of micromotion human target, in which the experiment scene plane is shown in Fig. 12(a). Furthermore, the micromotion human target range profile plane is shown in Fig. 13. The time delays of two paths are extracted from range profile. According to the proposed method, the positions of the micromotion human are obtained, as shown in Fig. 19. It is clear that the locations of the target are presented. The human sways back and forth during the data collection, which results in the expansion of the range profile trajectories and the positioning results. The measured mean position of the target is  $(-1.75 \text{ m}, 2.92 \text{ m})$ , while the

deviation between the initial position and the mean position is about 0.09 m. Thus, the 2-D position of the target can be calculated by using the proposed algorithm.

Next, for the case of moving target, the experiment scene plane is shown in Fig. 12(b). From this figure, the moving target range profile plane is shown in Fig. 14. We can see that the range profile trajectories correspond to *Path-1* and *Path-2*. Then, the localization results are acquired using the proposed method based on the calculated path time delay, as shown in Fig. 20. It can be seen that the calculated target positions are roughly located along a straight line and there is a good agreement between the estimated and the true target positions. Due to the influence of environmental noise and measurement errors, there are some fluctuations in the target trajectory. Considering the expansion characteristics and the body swing of the human target, the above errors are acceptable in practice. Thus, the proposed approach can be applied to obtain the coordinates of hidden target.

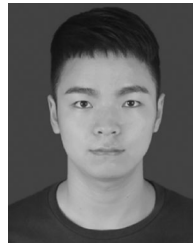
#### IV. CONCLUSION

A phenomenon of EM wave diffraction propagation in the single rectangular corner of the building scene is described in this article. Specifically, the possibility of detection of targets hidden behind the corner of the building with a UWB radar by exploiting EM wave diffraction propagation is analyzed based on established the single rectangular building corner diffraction echo models. Suppose that a target is located around a building corner and the geometric structure is known *a priori*. NLOS hidden target localization algorithm based on SISO UWB radar is proposed. Finally, several experimental results validate the effectiveness of the proposed algorithm. As the extension of this

article, possible future research tracks might concern the study of the multiple hidden targets localization for unknown building layout in more complicated scenarios.

## REFERENCES

- [1] M. Leigsnering, F. Ahmad, M. Amin, and A. Zoubir, "Parametric dictionary learning for sparsity-based TWRI in multipath environments," *IEEE Trans. Aerosp. Electron. Syst.*, vol. 52, no. 2, pp. 532–547, May 2016.
- [2] L. Qiu, T. Jin, B. Lu, and Z. Zhou, "An isophase-based life signal extraction in through-the-wall radar," *IEEE Geosci. Remote Sensor Lett.*, vol. 14, no. 2, pp. 193–197, Dec. 2016.
- [3] G. Gennarelli, R. Solimene, F. Soldovieri, and M. Amin, "Three-dimensional through-wall sensing of moving targets using passive multistatic radars," *IEEE J. Sel. Topics Appl. Earth Observ. Remote Sensor*, vol. 9, no. 1, pp. 141–148, Jun. 2015.
- [4] Y. Jia *et al.*, "Multipath ghost suppression based on generative adversarial nets in through-wall radar imaging," *Electronics*, vol. 8, no. 9, Jun. 2019, Art. no. 626.
- [5] H. Li, G. Cui, L. Kong, G. Chen, M. Wang, and S. Guo, "Robust human targets tracking for MIMO through-wall radar via multi-algorithm fusion," *IEEE J. Sel. Topics Appl. Earth Observ. Remote Sensor*, vol. 12, no. 4, pp. 1154–1164, Mar. 2019.
- [6] S. Guo, G. Cui, L. Kong, and X. Yang, "An imaging dictionary based multipath suppression algorithm for through-wall radar imaging," *IEEE Trans. Aerosp. Electron. Syst.*, vol. 54, no. 1, pp. 269–283, Sep. 2018.
- [7] A. Sume *et al.*, "Radar detection of moving targets behind corners," *IEEE Trans. Geosci. Remote Sensor*, vol. 49, no. 6, pp. 2259–2267, Jan. 2011.
- [8] T. Johansson *et al.*, "Radar measurements of moving objects around corners in a realistic scene," in *Proc. SPIE*, May 2014, vol. 9077, Art. no. 90771Q.
- [9] A. Sume, M. Gustafsson, and A. Janis, "Radar detection of moving objects around corners," in *Proc. SPIE*, Apr. 2009, vol. 7308, pp. 73080V-1–73080V-18.
- [10] M. Gustafsson, "Positioning of objects behind corners using X-band radar," in *Proc. 30th URSI Gen. Assem. Sci. Symp.*, Istanbul, Turkey, Aug. 2011, pp. 1–4.
- [11] T. Johansson, A. Andersson, M. Gustafsson, and S. Nilsson, "Positioning of moving non-line-of-sight targets behind a corner," in *Proc. 13th Eur. Radar Conf.*, London, U.K., Oct. 2016, pp. 181–184.
- [12] M. Gustafsson, A. Andersson, T. Johansson, S. Nilsson, A. Sume, and A. Orbom, "Extraction of human micro-doppler signature in an urban environment using a "sensing-behind-the-corner" radar," *IEEE Geosci. Remote Sensor Lett.*, vol. 13, no. 2, pp. 187–191, Dec. 2015.
- [13] M. Gustafsson, A. Andersson, T. Johansson, R. Jonsson, N. Karlsson, and S. Nilsson, "Micro-Doppler extraction of a small UAV in a non-line-of-sight urban scenario," in *Proc. SPIE*, May 2017.
- [14] P. Setlur, T. Negishi, N. Devroye, and D. Erricolo, "Multipath exploitation in non-los urban synthetic aperture radar," *IEEE J. Sel. Topics Signal Process.*, vol. 8, no. 1, pp. 137–152, Feb. 2013.
- [15] L. Fertig, J. Baden, and J. Guerci, "Knowledge-aided processing for multipath exploitation radar," *IEEE Aerosp. Electron. Syst. Mag.*, vol. 32, no. 10, pp. 24–36, Dec. 2017.
- [16] R. Zetik, M. Eschrich, S. Jovanoska, and R. Thoma, "Looking behind a corner using multipath-exploiting UWB radar," *IEEE Trans. Aerosp. Electron. Syst.*, vol. 51, no. 3, pp. 1916–1926, Sep. 2015.
- [17] K. Thai, O. Rabaste, J. Bosse, and T. Chonavel, "GLRT particle filter for tracking NLOS target in around-the-corner radar," in *Proc. IEEE Int. Conf. Acoust., Speech, Signal Process.*, Calgary, AB, Canada, Apr. 2018, pp. 3216–3220.
- [18] K. Thai *et al.*, "Around-the-corner radar: Detection and localization of a target in non-line of sight," in *Proc. IEEE Radar Conf.*, Seattle, WA, USA, May 2017, pp. 0842–0847.
- [19] K. Thai, O. Rabaste, J. Bosse, and D. Poullin, "Detection-localization algorithms in the around-the-corner radar problem," *IEEE Trans. Aerosp. Electron. Syst.*, vol. 55, no. 6, pp. 2658–2673, Dec. 2019.
- [20] Q. Zhao, G. Cui, S. Guo, W. Yi, L. Kong, and X. Yang, "Millimeter wave radar detection of moving targets behind a corner," in *Proc. IEEE Int. Conf. Inf. Fusion.*, Cambridge, U.K., Jul. 2018, pp. 2042–2046.
- [21] S. Fan, G. Cui, S. Guo, L. Kong, X. Yang, and X. Yuan, "Corner target positioning with unknown walls' positions," *J. Eng.*, vol. 2019, no. 19, pp. 6143–6146, Oct. 2019.
- [22] S. Fan *et al.*, "Moving target localization behind L-shaped corner with a UWB radar," in *Proc. IEEE Radar Conf.*, Boston, MA, USA, Apr. 2019, pp. 1–5.
- [23] S. Li *et al.*, "NLOS target localization with a UWB radar," in *Proc. IEEE Radar Conf.*, Boston, MA, USA, Apr. 2019, pp. 1–5.
- [24] J. Liu, Y. Jia, L. Kong, X. Yang, and Q. Liu, "MIMO through-wall radar 3-D imaging of a human body in different postures," *J. Electro-Magn. Appl.*, vol. 30, no. 7, pp. 849–859, Apr. 2016.
- [25] G. Cui, L. Kong, and X. Yang, "Reconstruction filter design for stepped-frequency continuous wave," *IEEE Trans. Signal Process.*, vol. 60, no. 8, pp. 4421–4426, May 2012.
- [26] M. Iskander and Z. Yun, "Propagation prediction models for wireless communication systems," *IEEE Trans. Microw. Theory Techn.*, vol. 50, no. 3, pp. 662–673, Aug. 2002.
- [27] M. Jacob, S. Priebe, R. Dickhoff, T. Ostmann, T. Schrader, and T. Kurner, "Diffraction in MM and sub-MM wave indoor propagation channels," *IEEE Trans. Microw. Theory Techn.*, vol. 60, no. 3, pp. 833–844, Jan. 2012.
- [28] A. Martone, K. Ranney, and R. Innocenti, "Automatic through the wall detection of moving targets using low-frequency ultra-wideband radar," in *Proc. IEEE Radar Conf.*, Washington, DC, USA, May 2010, pp. 39–43.
- [29] H. Brunzell, "Detection of shallowly buried objects using impulse radar," *IEEE Trans. Geosci. Remote Sensor*, vol. 37, no. 2, pp. 875–886, Mar. 1999.
- [30] C. Warren *et al.*, "A CUDA-based GPU engine for gprMax: Open source FDTD electromagnetic simulation software," *Comput. Phys. Commun.*, vol. 237, pp. 208–218, Apr. 2019.
- [31] A. Di Vito and G. Morreti, "Probability of false alarm in CA-VFAR device downstream from linear-law detector," *Electron. Lett.*, vol. 25, no. 25, pp. 1692–1693, Dec. 1989.
- [32] D. Crouse, "A general solution to optimal fixed-Gain ( $\alpha$ - $\beta$ - $\gamma$  etc.) filters," *IEEE Signal Process Lett.*, vol. 22, no. 7, pp. 901–904, Dec. 2014.



**Songlin Li** received the B.S. degree from Chengdu University of Technology, Chengdu, China, in 2018. He is currently working toward the M.S. degree with the School of Information and Communication Engineering, University of Electronic Science and Technology of China, Chengdu, China.

His research interests include NLOS target detection in urban environment.



**Guolong Cui** (Senior Member, IEEE) received the B.S. degree in electronic information engineering, the M.S. and Ph.D. degrees in signal and information processing from the University of Electronic Science and Technology of China (UESTC), Chengdu, China, in 2005, 2008, and 2012, respectively.

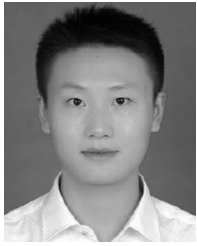
From January 2011 to April 2011, he was a Visiting Researcher with the University of Naples Federico II, Naples, Italy. From June 2012 to August 2013, he was a Postdoctoral Researcher with the Department of Electrical and Computer Engineering, Stevens Institute of Technology, Hoboken, NJ, USA. From September 2013 to July 2018, he was an Associate Professor with UESTC, where since August 2018, he has been a Professor. His current research interests include cognitive radar, array signal processing, MIMO radar, and through-the-wall radar.



**Shisheng Guo** (Member, IEEE) received the B.S. degree in communication engineering from Nanchang Hangkong University, Nanchang, China, in 2013, and the Ph.D. degree in signal and information processing from the University of Electronic Science and Technology of China (UESTC), Chengdu, China, in 2019.

He is currently an Associate Researcher with School of Information and Communication Engineering, UESTC, Chengdu, China. His research interests include through-the-wall radar imaging, signal analysis, and NLOS target detection.





**Chao Jia** received the M.S.E.E degree from the University of Electronic Science and Technology of China (UESTC), Chengdu, China, in 2013. He is currently working toward the D.E. degree with the School of Information and Communication Engineering, UESTC.

His research interests include NLOS target detection in urban environment and radar signal processing.



**Xiaobo Yang** received the B.S. and M.S. degrees in electronic engineering from the University of Electronic Science and Technology of China (UESTC), Chengdu, China, in 1986 and 1988, respectively.

He is currently a Professor with the School of Information and Communication Engineering, UESTC. His research interests include multiple-input multiple-output radar, through-the-wall radar, statistical signal processing, and intelligent signal processing.



**Lingjiang Kong** (Senior Member, IEEE) received the B.S. degree in electronic engineering, the M.S. and Ph.D. degrees in signal and information processing from the University of Electronic Science and Technology of China (UESTC), Chengdu, China, in 1997, 2000, and 2003, respectively.

From September 2009 to March 2010, he was a Visiting Researcher with the University of Florida. He is currently a Professor with the School of Information and Communication Engineering, UESTC. His research interests include multiple-input multiple-output radar, through-the-wall radar, statistical signal processing, and intelligent signal processing.